Brain, Behavior, & Immunity - Health 40 (2024) 100826

Contents lists available at ScienceDirect

Brain, Behavior, & Immunity - Health

journal homepage: www.editorialmanager.com/bbih/default.aspx

A small molecule p38α MAPK inhibitor, MW150, attenuates behavioral deficits and neuronal dysfunction in a mouse model of mixed amyloid and vascular pathologies

Hilaree N. Frazier [a,1], David J. Braun [a,b,1], Caleb S. Bailey [a], Meggie J. Coleman [a], Verda A. Davis [a], Stephen R. Dundon [c], Christopher J. McLouth [d], Hana C. Muzyk [a], David K. Powell [b,c], Colin B. Rogers [a], Saktimayee M. Roy [e], Linda J. Van Eldik [a,b,*]

[a] Sanders-Brown Center on Aging, University of Kentucky, Lexington, KY, 40536, USA
[b] Department of Neuroscience, University of Kentucky, Lexington, KY, 40536, USA
[c] Magnetic Resonance Imaging & Spectroscopy Center, University of Kentucky, Lexington, KY, 40536, USA
[d] Department of Biostatistics, University of Kentucky, Lexington, KY, 40536, USA
[e] Department of Pharmacology, Northwestern University, Chicago, IL, 60611, USA

ARTICLE INFO

Keywords:
Alzheimer's disease
VCID
Hyperhomocysteinemia
p38 MAPK
Hippocampus
neuroinflammation
Synaptic plasticity
LTP

ABSTRACT

Background: Inhibition of p38 alpha mitogen activated protein kinase (p38α) has shown great promise as a treatment for Alzheimer's disease (AD) in preclinical tests. However, previous preclinical studies were performed in "pure" models of AD pathology. A vast majority of AD patients have comorbid dementia-contributing pathologies, particularly some form of vascular damage. The present study therefore aimed to test the potential of p38α inhibition to address dysfunction in the context of comorbid amyloid and vascular pathologies.

Methods: An amyloid overexpressing mouse strain (5xFAD) was placed on an 8-week long diet to induce the hyperhomocysteinemia (HHcy) model of small vessel disease. Mice were treated with the brain-penetrant small molecule p38α inhibitor MW150 for the duration of the HHcy diet, and subsequently underwent behavioral, neuroimaging, electrophysiological, or biochemical/immunohistochemical analyses.

Results: MW150 successfully reduced behavioral impairment in the Morris Water Maze, corresponding with attenuation of synaptic loss, reduction in tau phosphorylation, and a partial normalization of electrophysiological parameters. No effect of MW150 was observed on the amyloid, vascular, or neuroinflammatory endpoints measured.

Conclusions: This study provides proof-of-principle that the inhibition of p38α is able to provide benefit even in the context of mixed pathological contributions to cognitive impairment. Interestingly, the benefit was mediated primarily via rescue of neuronal function without any direct effects on the primary pathologies. These data suggest a potential use for p38 inhibitors in the preservation of cognition across contexts, and in particular AD, either alone or as an adjunct to other AD therapies (*i.e.* anti-amyloid approaches). Future studies to delineate the precise neuronal pathways implicated in the benefit may help define other specific comorbid conditions amenable to this type of approach or suggest future refinement in pharmacological targeting.

Abbreviations: AD, Alzheimer's disease; Aβ, amyloid beta; VCID, vascular contributions to cognitive impairment and dementia; HHcy, hyperhomocysteinemia; HPC, hippocampus; WT, wild-type; MD, mixed disease; Veh, saline vehicle; MWM, Morris water maze; NSR, novel-spatial recognition; IHC, immunohistochemistry; IF, immunofluorescence; WB, Western immunoblot; LTP, long-term potentiation; PP, paired-pulse; I/O, input/output; EPSP, excitatory post-synaptic potential; ACSF, artificial cerebrospinal fluid; SEM, standard error of the mean; SWI, susceptibility weighted imaging; DTI, diffusion tensor imaging; ROI, region of interest; FOV, field of view.

* Corresponding author. Sanders-Brown Center on Aging, University of Kentucky, Lexington, KY, 40536, USA.
E-mail address: linda.vaneldik@uky.edu (L.J. Van Eldik).

[1] These authors contributed equally to this work.

https://doi.org/10.1016/j.bbih.2024.100826
Received 18 July 2024; Accepted 20 July 2024
Available online 23 July 2024

1. Introduction

Although the pathological hallmarks of Alzheimer's disease (AD) are the presence of amyloid (Aβ) plaques and neurofibrillary tau tangles, other pathological changes are also present and known to significantly contribute to cognitive decline. Of these comorbidities, vascular contributions to cognitive impairment and dementia (VCID) is among the most clinically relevant, given that 80% of AD patients were found to have concurrent vascular pathology at the time of autopsy (Toledo et al., 2013) and the combination of AD and small vessel pathology has been reported to significantly increase the likelihood of developing dementia (Kapasi and Schneider, 2016). Despite this, most preclinical studies of AD have been performed in transgenic mouse models with only Aβ and/or tau pathology. Due to the inherent limitations of these "pure" AD pathology models, the molecular mechanisms underlying the functional changes that result from this mixed pathology, and how to effectively target these changes, remain unclear.

Neuroinflammation is a commonly reported feature in both VCID and AD (Heppner et al., 2015; Heneka et al., 2015; Grammas, 2011; Lenart et al., 2016; Van Eldik et al., 2016; Andreasson et al., 2016), representing an attractive therapeutic target. Recently, we have found that inhibition of neuroinflammatory pathways can provide benefit in the mixed AD and vascular neuropathological context. Administration of a small-molecule anti-inflammatory drug MW151 partially rescued memory impairment, reduced IL-1β levels, and normalized hippocampal markers of metabolism and astrocyte activation in a model of mixed AD and vascular pathology similar to the one used here (Braun et al., 2022). While encouraging, the precise molecular target of MW151 remains unknown, making it difficult to identify the particular pathways that may be mediating these improvements. The p38α mitogen-activated protein kinase (MAPK) is expressed in all CNS cell-types and is a well-known regulator of neuroinflammatory processes across various animal models of disease (Bachstetter et al., 2011; Bachstetter and Van Eldik, 2010). Several studies investigating the effects of p38α inhibition on neuroinflammation have shown promising results. In fact, previous work from our lab reported that pharmacologic inhibition of p38α using MW150, a novel, highly specific drug candidate currently undergoing clinical trials, reduced markers of neuroinflammation and improved cognitive performance in several distinct AD mouse models (Zhou et al., 2017; Roy et al., 2015, 2019). A different p38α inhibitor, Neflamapimod, is currently in early-stage AD clinical trials (Prins et al., 2021; Scheltens et al., 2018). Still, it is not yet clear whether p38α inhibition will be effective in models of mixed pathology. Using 5xFAD mice (Oakley et al., 2006) with diet-induced hyperhomocysteinemia (HHcy)—a known AD risk factor associated with small vessel damage, microglial activation, synaptic impairment, and cognitive dysfunction (Sudduth et al., 2014)—we tested if MW150 administration could attenuate aspects of comorbid vascular and/or Aβ neuropathology in this model of mixed disease (MD).

2. Materials and methods

Experiments were carried out across three separate animal studies, each with associated methods described in detail below and summarized in Fig. 1. A supplemental spreadsheet with the full dataset is included for each respective experiment (**Supplement 1**). Additional dietary information is included in **Supplement 2**.

2.1. Experiment 1: effects of MW150 on hippocampal-dependent spatial memory impairment

Animals and model: The goal of this study was to test whether MW150 might preserve hippocampal-dependent learning in a model of mixed disease (MD). This experiment was performed by the In Vivo Pharmacology Services of the Jackson Laboratories, in accordance with both the Jackson Laboratories and University of Kentucky IACUC protocols. Female C57BL/6J mice were used, either heterozygous carriers of the 5xFAD mutations (034848-JAX) (Oakley et al., 2006), or the

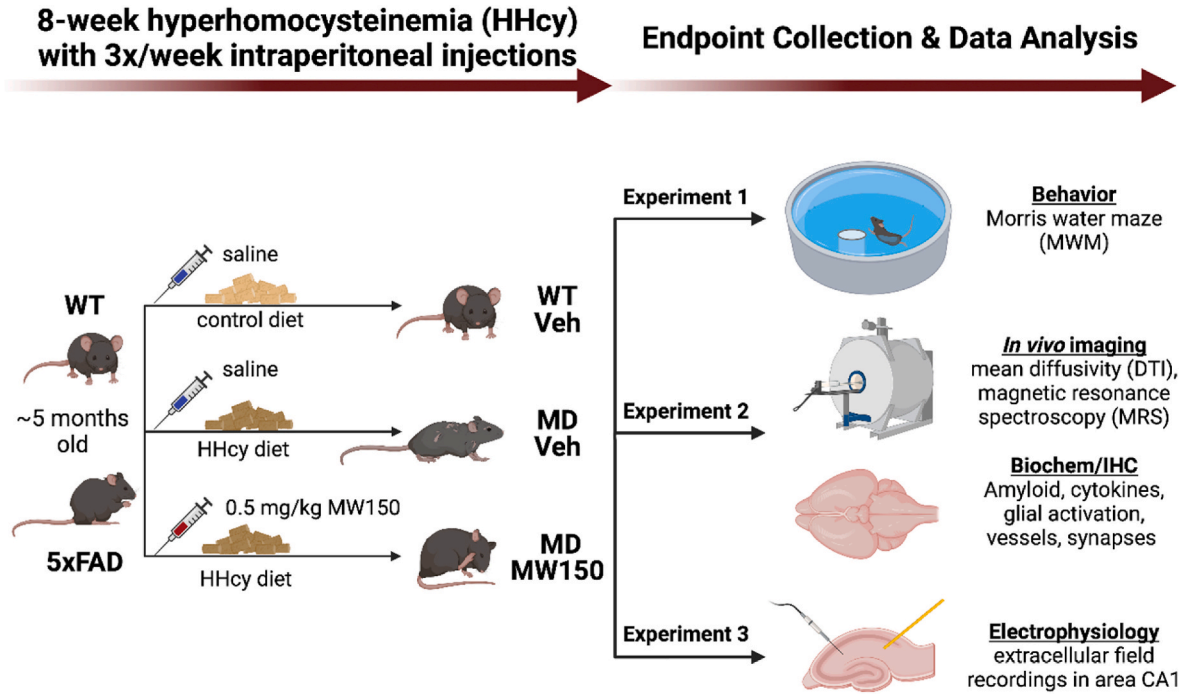

Fig. 1. Experimental model and endpoints. The results contained in this manuscript were performed across three separate experiments, each utilizing the same "mixed disease" (MD) model of comorbid amyloid and vascular pathologies. The former was generated by use of the 5xFAD strain, and the latter by a dietary method of inducing hyperhomocysteinemia (HHcy). This was performed after the mice had developed significant amyloid pathology by starting them on a B-vitamin deficient diet at around 5 months of age. Mice were maintained on this diet for 8 weeks, during which time they received 3x per week injections of MW150 or saline vehicle, prior to undergoing the endpoints described. Only female mice were used.

non-carrier WT littermate controls. To create the mixed disease (MD) model combining amyloid and vascular pathologies, the 5xFAD carriers at 22 weeks of age were placed on a diet (Teklad TD.200796) deficient in vitamins B6, B9, and B12 and with excess methionine to induce hyperhomocysteinemia (HHcy) (Sudduth et al., 2013) (see **Supplement 2** for nutrient detail). Mice were kept on HHcy diet for 8 weeks, during which time they were injected 3x per week IP with MW150 or saline vehicle (Fig. 1). The WT control mice were on a diet nutritionally matched to the HHcy but with normal vitamin and methionine levels (Teklad TD.200795) and injected with an equivalent volume of saline. At the conclusion of the 8 weeks of diet and drug administration, all mice were returned to standard rodent chow 48 h prior to testing in the Morris Water Maze. A total of 12 mice were included in each of four groups: WT mice on control diet injected with saline vehicle (WT Veh), 5xFAD mice on HHcy diet injected with saline (MD Veh), 5xFAD mice on HHcy diet injected with 0.5 mg/kg MW150 (MD 0.5 MW150), and 5xFAD mice on HHcy diet injected with 2.5 mg/kg MW150 (MD 2.5 MW150). Dosing was adjusted to deliver 0.5 or 2.5 mg/kg MW150 in 200 μL per mouse, with 10X stocks provided for 2.5 mg/kg (6.428 mg/mL) and 0.5 mg/kg (1.286 mg/mL) injections, each diluted 1:10 in saline prior to administration.

Morris Water Maze (MWM): The MWM was performed by blinded technicians in a circular mouse pool (Med Associates Inc., ENV-594M DB) surrounded by fixed extra-maze cues, and analyzed by an overhead camera interfaced with the Noldus Ethovision XT 15 tracking system. The water was maintained at a temperature of 23–25 °C and made opaque by addition of non-toxic white tempera paint. During the acquisition phase, mice were trained for five consecutive days, with four trials per day, each trial separated by a 20 min inter-trial interval. The animal was placed into the pool from one of each of four start points in a randomized, non-repeating sequence on each day. The location of the platform was always in the center of the same target quadrant. Mice were allowed to swim from the release point for up to 60 s or until finding the platform. Mice that failed to locate the platform in this timeframe were guided to it by the experimenter. After reaching the platform, all mice were allowed to remain for 15 s prior to removal from the apparatus. Latency to reach the platform was averaged per mouse per day. Twenty-four hours after the final acquisition session, all mice underwent a probe session with the platform removed from the pool. All mice were released from the same randomized start point and allowed to swim freely for 60 s. The percent of time in the target quadrant was recorded. Twenty minutes after the probe test, all mice underwent a cued test to assess sensorimotor ability and motivation. The platform was situated in the same quadrant as in the acquisition phase, but about 1 cm above the water with a flag attached and the extra-maze cues removed, ensuring the mice could locate the platform using a local visual stimulus rather than relying on spatial orientation. The cued test maximum duration was 60 s and latency to reach the platform was measured. Finally, two weeks after the cued test, a retention test was conducted consisting of two trials 20 min apart. The platform was situated at the same position as during the acquisition phase and mice were given 60 s to find the platform per trial. Latency to reach the platform was averaged over the two retention trials per mouse.

Statistical analyses: Linear mixed models were used to account for repeated testing of mice across time. Condition, trial number, and their interaction were included as fixed effects with a random intercept for each mouse. In order to adjust for multiple comparisons, follow-up tests for significant effects of Condition were employed using Dunnett's test with MD Veh as the control condition (Dunnett,1955) and the Bonferroni procedure (Dunn, 1961) was used to correct for trial number. Learning curves are displayed as the standard mean latency ± standard error of the mean (SEM) to find the platform and were analyzed by PROC MIXED in SAS version 9.4. Cued and retention trials were analyzed by non-parametric Kruskal-Wallis tests followed by Dunn's post-hoc comparisons in GraphPad Prism version 10.1.1 (Prism). Probe trial data were not censored and met appropriate assumptions for parametric testing (normality of residuals, equal variance, independent observations) so were analyzed by one-way ANOVA followed by Sidak's multiple comparison testing, also in Prism. All figure graphs were generated in Prism.

2.2. Experiment 2: effects of MW150 on neuroimaging and neuropathology endpoints

Animals and model: This experiment was performed at the University of Kentucky in accordance with the applicable University of Kentucky IACUC protocol. As in experiment 1, 22 week old female C57BL/6J 5xFAD and WT littermates were used, placed on either control (Teklad TD.01636) or HHcy diets (Teklad TD.97345) (Braun et al., 2022) for 8 weeks to generate the MD model. MW150 (0.5 mg/kg) or saline vehicle was administered IP 3x per week as in Experiment 1. After the 8 weeks of diet and injections, mice underwent magnetic resonance imaging within 48 h of their final injection and were euthanized 72 h after their final injection. Mice were maintained on the HHcy or control diets until euthanasia. For the WT, MD Veh, and MD 0.5 MW150 groups, the mouse numbers were 10, 13, and 12, respectively.

Magnetic resonance imaging (MRI) acquisition and analyses: All imaging was performed at the University of Kentucky Magnetic Resonance Imaging and Spectroscopy Center (MRISC) on a 7T Bruker BioSpec MRI system. As previously described (Braun et al., 2022), all mice were anesthetized with 5% isoflurane and transferred to the scanner bed with heating pad, where anesthetic depth was maintained in a ~1–2% isoflurane and air mixture using a nose cone. Imaging was performed after mice reached a stable temperature (35–36 °C) and respiratory rate (70–100 breaths/min). A whole-body volume coil was used for transmission and a mouse brain surface coil for receiving. T2-weighted structural images were acquired with a field of view (FOV) = 20 mm × 20 mm, matrix = 256 x 256; slice thickness = 0.6 mm, 15 slices, repetition time (TR) = 3000 ms, echo time (TE) = 33 ms and used primarily for anatomical alignment of the subsequent scans.

Susceptibility weighted imaging (SWI) was performed with the following parameters: FOV 20 mm × 20 mm, matrix = 290 x 290; slice thickness = 0.5 mm, 13 slices, TR = 438.7 ms, TE = 18 ms, 3 averages, flip angle = 30°. Images were opened using FSLeyes and dark spots on the SWI scans were judged and manually counted by a blinded investigator. Given the bilateral nature, relatively consistent localization, and anatomical arrangement, these spots appeared to largely reflect venous blood supply in cross-section. Further, the SWI data showed no relationship to gold-standard microbleed quantification by Prussian Blue staining (see Immunohistochemical staining and imaging section, below) indicating that the SWI scan lacked the spatial resolution to detect the small microbleeds present in this model; therefore SWI was not analyzed across groups.

The diffusion tensor imaging (DTI) scan was performed as a spin-echo EPI, with 4 RF segments with the following scan parameters: TR = 2000 ms, TE = 20 ms, slice thickness = 0.8 mm, 5 total slices, total scan time = 4 min 40 s, FOV = 18 mm × 15 mm, matrix = 128 x 128, number of diffusion directions = 30, strength of diffusion encoding = 650 s/mm^2, number of zero diffusion measurements = 5, and fat saturation. Hippocampal mean diffusivity and fractional anisotropy (FA) measurements were taken from a single slice through the dorsal hippocampus, anatomically matched across mice and manually outlined in FSLeyes by a blinded investigator.

For magnetic resonance spectroscopy (MRS), a 5.2× 1.8 × 2.8 mm^3 voxel was placed around the bilateral hippocampus for water-suppressed MRS measurement: TR = 2500 ms, TE = 16.5 ms, 256 scans averaged. This was followed by a scan without water suppression, 10 averages. Water-suppressed and unsuppressed scans were processed using LCModel (Provencher, 1993). All metabolites are expressed as a ratio of the total creatine (Cr + PCr) signal. Analyzed metabolite peak values with estimated Cramér-Rao lower bounds >15% were excluded from analysis. If a metabolite was excluded on this basis from more than

20% of the mice, then it was considered not reliably detectable and therefore not analyzed across groups. For metabolites with both individual and combined peaks (e.g. NAA + NAAG) only the combined peak was analyzed.

Humane euthanasia and tissue harvest: Mice were deeply anesthetized by 5% isoflurane, euthanized by exsanguination with transcardial perfusion of 50 mL 1X PBS (Cellgro Mediatech, #46-013-CM), and tissue collected as previously described (Braun et al., 2022). Briefly, brain hemispheres were bisected at the midline and the right hemisphere immediately post-fixed in 4% PFA for ~24 h and cryopreserved at 4 °C in 30% sucrose for at least 5 days prior to sectioning. The hemisphere was sectioned coronally at 30 μm thickness on a freezing microtome and stored at −20 °C in cryoprotectant as previously described (Braun et al., 2023). For biochemical endpoints, hippocampus was dissected out, laid flat, and bisected lengthwise prior to the two pieces being flash frozen in liquid nitrogen, and stored at −80 °C before processing.

Biochemical endpoints: For cytokine measurements, one piece of hippocampus was fractionated to enrich for cytosolic proteins as described (Braun et al., 2023). Briefly, tissue was homogenized in 1X PBS lysis buffer (1:20 w/v) containing 0.2X Halt Protease Inhibitor Cocktail with 0.5 mM EDTA (Pierce, #78442) and 1 mM PMSF using a Bead Ruptor 24 homogenizer without beads (Omni International Inc., Kennesaw, GA). Homogenates were centrifuged (12000×*g*, 20 min, 4 °C) and supernatants collected and run on the V-PLEX Mouse Cytokine 19-Plex Kit (MSD, #K15255D) according to manufacturer's instructions with the following changes to increase assay sensitivity: 50 μL of supernatant with 25 μL of assay diluent buffer was loaded per well and plates were shaken overnight at 4 °C rather than at room temperature for 1 h after sample loading. Plates were read by an MSD Quickplex SQ120 plate reader and analyzed by Discovery Workbench 4.0 Software. Cytokines in supernatant were normalized to protein loaded per sample as determined by BCA assay and are expressed as (pg/ml)/mg. Analytes not detected in ≥20% of the samples were excluded from the final analyses.

Immunohistochemical staining, imaging, and quantification: For measures of microhemorrhages, olfactory bulb and cerebellum were removed, and free-floating coronal sections through the remaining extent of the brain were taken spaced approximately 300 μm apart (7-23 sections per animal, n = 11–13 mice per group). These were stained using a Prussian blue (PB) iron staining kit with nuclear fast red counterstain (Abcam, #ab150674) according to manufacturer instructions. Slides were then mounted and coverslipped using DPX mounting medium (Electron Microscopy Sciences, #13512). To measure microglial morphology, blocked sections (10% goat serum and 0.2% TX-100 in PBS for 1 h) were incubated in 1:1000 rabbit anti-IBA1 primary antibody (FUJIFILM Wako Shibayagi, #019–19741) overnight at 4 °C, followed by 1:1000 anti-rabbit biotin secondary antibody (Vector Labs, #BA-1000) and Vectastain Elite ABC kit (Vector Labs, #PK-6100). IBA1-stained sections were developed with 0.05% (w/v) 3,3′-diaminobenzidine tetrahydrochloride hydrate (MilliporeSigma, #D5637) and counterstained in Mayer's modified hematoxylin solution (Abcam, #ab220365) for visualization of nuclei prior to mounting and coverslipping with DPX mounting medium. PB and IBA1 slides were imaged on an Aperio ScanScope XT digital slide scanner using a 20× magnification and analyzed in HALO v.3.5 software (Indica Labs). For Prussian blue slides, the Random Forest v2 classifier algorithm (resolution 2.03 μm/px, min object size 200 μm^2) was used to identify individual objects positive for PB stain across the entire section, which were then visually confirmed by a separate blinded investigator. For IBA1 measures, the hippocampus was manually outlined by a blinded investigator and analyzed using the HALO Microglial Activation v1.4 algorithm with adjusted signal intensity and size thresholds (contrast threshold 0.45, min process OD 0.35, min cell body diameter 3.5 μm, max process radius 12 μm, max fragmentation length 13 μm, activation process thickness 2.7 μm) in order to identify activated versus homeostatic IBA1+ cells.

For GFAP, dystrophin, and amyloid staining the following antibody pairs were used: 1:2000 rat anti-GFAP (ThermoFisher, #13–0300) with 1:750 anti-rat AlexaFluor 405 (Thermo, #A48261), 1:1000 rabbit anti-dystrophin (Abcam, #ab15277) with 1:500 anti-rabbit AlexaFluor 594 (Thermo, #A32740), and 1:800 AlexaFluor 488-conjugated mouse anti-Aβ 6E10 primary (BioLegend, #803013). For synaptic endpoints, 1:120 rabbit anti-PSD95 (Abcam #ab238135) with 1:1000 anti-rabbit AlexaFluor 488 (Thermo, #A11034), and 1:100 chicken anti-synaptophysin (Synaptic Solutions, #101006(SY)) with 1:500 anti-chicken AlexaFluor+ 405 (Thermo #A48260) were used. Fluorescently stained sections were mounted and coverslipped with EverBright TrueBlack Hardset medium containing a Cy5 (640 nm) fluorescent nuclear stain (Biotium, #23016).

For the GFAP, dystrophin, and amyloid analyses, slides containing 2–5 tissue sections were imaged per animal using a Nikon BioPipeline Slide scanner (Nikon, Tokyo, Japan) and 10× Plan Apo lambda objective. Images were stitched together and post-processed with denoise.ai and 2D deconvolution in NIS Elements v5.4 (Nikon), then imported into HALO imaging software (Indica Labs) for analysis. Hippocampal regions were manually outlined in HALO by a blinded investigator, followed by quantification of GFAP (DAPI), dystrophin (TxRed), and 6E10 (FITC) staining using the HALO Object Colocalization FL v.2.1.4 algorithm with adjusted minimum signal intensity thresholds (DAPI 700; TxRed 550; FITC 1000). To avoid including erroneous imaging artifacts or regions of high background signal in the analysis, the algorithm was also adjusted to limit the inclusion of positively stained objects to only those within a defined size range ([in μm^2] DAPI 5–34,865; FITC 50–100,000; TxRed 30–4000). To derive measures of astrocyte, vessel, and plaque numbers, object counts were first normalized to the total hippocampal area within the section prior to analysis. Sections were then averaged to derive 1 value per measure for each animal.

For assessment of synaptophysin and PSD95, confocal imaging was performed by a blinded investigator on fluorescently stained sections containing hippocampus (1 per animal, randomly selected) using an A1R-HD confocal microscope controlled by NIS Elements software (Nikon). Briefly, Z-stack images across 2.5 μm (step size of 0.1 μm) were taken in hippocampal areas CA1 and CA3 (1 image per area) at 1024x1024 resolution using a 60× oil-immersion objective with a 2× digital zoom for final magnification of 120×. Z-stacks were then post-processed using denoise. ai and 3D deconvolution prior to analysis. Individual puncta positively stained for either synaptophysin (DAPI) or PSD95 (FITC) were identified using the NIS-Elements colocalization algorithm with minimum signal intensities set to 126 for DAPI, 2080 for FITC and max puncta size at 25 μm. Regions of interest (ROIs) containing colocalized synaptophysin and PSD95 puncta directly touching one another within the 3D planes were also quantified as a measure of synapse number.

Western immunoblots: To determine the effect of p38α inhibition on tau levels and phosphorylation, we performed a Western immunoblot using hippocampus (HPC) tissue samples from WT and MD mice (n = 7–8 per group). Briefly, tissue samples were homogenized in 1:10 w/v T-PER™ Tissue Protein Extraction buffer (Thermo, #78510) containing 0.1X Halt protease inhibitor cocktail (Thermo, #78442), 1X phosphatase inhibitor cocktail (Cell Signaling, #5870), and 1 mM EDTA (Thermo, #78442) using a Bead Ruptor 24 homogenizer. After centrifugation (12000×*g*, 20 min, 4 °C), supernatants were collected and assessed for protein concentration using a BCA assay, then frozen at −20 °C. On the day of the experiment, lysates were thawed on ice and diluted with the appropriate amount of T-PER buffer needed to reach a protein concentration of 0.889 μg/μL. Samples were then mixed with loading buffer (Li-Cor, #28–40004) containing 0.1% 2-mercaptoethanol and heated on a heat block at 70 °C for 10 min. After cooling to room temperature (RT) for 15 min, samples were loaded into 4–12% gradient gel (Thermo, #WG1401BOX) and run at 200V for 40 min using an XCell4 electrophoresis chamber (Thermo, #WR0100). Once finished, gels were removed and samples were transferred to a nitrocellulose membrane using an iBlot® transfer device (Thermo, #IB1001). After

blocking in Intercept® (TBS) Blocking Buffer (Li-Cor, #927–60001) at RT for 1 h, the membrane was incubated in Revert™ 520 Total Protein Stain (Li-Cor, #926–10011) and imaged on the Li-Cor Odyssey M fluorescent imager at 520 nm. The membrane was then de-stained (Li-Cor, #826–19012), probed for total tau (1:2000 mouse anti-tau TAU5 primary [Thermo, #AHB0042] with 1:20000 IRDye 800CW goat anti-mouse IgG secondary [Li-Cor, #926–32210]) and Thr231 phosphorylated tau (1:4000 rabbit anti-tau phospho T231 primary [Abcam, #ab151559] with 1:20000 IRDye 680CW goat anti-rabbit IgG secondary [Li-Cor, #926–68071]), and visualized on the Li-Cor Odyssey M at 800 and 700 nm, respectively. Quantification of total protein stain and the two target bands of interest was performed in Li-Cor Empiria Studio® software using raw, unaltered images. For presentation purposes, images were adjusted for brightness/contrast levels to improve visual clarity. For measures of HPC tau levels, raw signals of total tau bands were normalized to Revert™ total protein stain signal of their corresponding lane, and are expressed as "total tau/protein load". For measures of Thr231 tau phosphorylation, raw signals of p-tau231 bands were normalized to raw signals of total tau bands to generate p-tau231/total tau ratios.

Statistical analyses: Data were screened and analyzed using SPSS 29.0 (IBM Corporation; Armonk, NY) and SAS 9.4 (SAS Institute; Cary, NC) or GraphPad Prism. DTI data failed assumptions of homoscedasticity and normality of residuals and so were analyzed by Kruskal-Wallis followed by Dunn's post-hoc tests. Western blot total tau/protein load and p-tau231/total tau variables were analyzed by linear regression; a natural log transformation of p-tau231/total tau resolved the normality of residuals violation for this specific analysis. Where required for the MRS and MSD ELISA variables, violations to model assumptions were resolved by nonlinear transformation of the dependent variables; however, all graphs show non-transformed data. The unstandardized B is reported for all analyses performed on non-transformed data, and the standardized β for transformed. For the MRS metabolites, multiple analysis of variance (MANOVA) was used to determine the omnibus effect of group condition across all MRS detectable metabolites. An exploratory multivariate multiple regression (MMR) procedure was used to determine the effect of group condition on each of the 14 MRS metabolites (SAS 9.4). The MSD cytokine panel resulted in 10 cytokines per mouse that met the analysis criteria, and MANOVA was similarly used to determine the omnibus effect of group condition across all cytokines, followed by MMR to determine the effect of group condition on the individual cytokines (SAS 9.4).

2.3. Experiment 3: effects of MW150 on neuronal function

Animals and model: This experiment was performed at the University of Kentucky in accordance with the applicable University of Kentucky IACUC protocol. The same groups were generated in the same manner as in experiment 2: WT, MD Veh, MD 0.5 MW150 and all mice remained on the assigned diet until euthanasia. Mice underwent behavioral testing for short-term memory in the novel spatial recognition (NRS) Y-maze variant on the same day as the final injection with MW150 or saline. Electrophysiology was performed within 48–96 h of the final injection. A total of 8–10 mice were included per group.

Novel spatial recognition (NSR) assay: The week prior to behavioral testing, mice were tunnel handled for 5 sessions as described (Braun et al., 2023) and habituated to the behavioral testing room for 1 h prior to testing. Mice were tested in a clear polycarbonate 3-armed Y-maze with light levels of ~5.8 lux. Distinct visual cues were placed at the distal wall of each arm: a black-and-white diagonal striped cue for the "start," a white plus sign on a black background for the "familiar," and a black circle on a white background for the "novel" arm. During the first 10 min familiarization phase, a removable panel was placed at the entrance of the novel arm to prevent access to that arm, and mice were placed in the start arm and allowed to freely explore the start and familiar arms. After a 10 min inter-trial interval, the panel blocking the novel arm in the Y-maze was removed and mice were placed back into the apparatus for a 5 min testing trial. ANY-maze tracking software recorded the percent time mice spent in each arm, as well as the average distance traveled and average speed. The apparatus was cleaned with 70% ethanol and dried after each trial. No deficits were detected in any of the groups (lack of preference for the novel arm), but the full data is included in **Supplement 1**.

Hippocampal slice electrophysiology: Extracellular field recordings in acute mouse brain slices were performed in a total of 18 mice (n = 8–10 per group, 1-4 slices per mouse) using methods adapted from (Mathis et al., 2011). Briefly, animals were deeply anesthetized using 5% isoflurane and euthanized via rapid decapitation. Whole mouse brains were then extracted and immediately placed into ice-cold, oxygenated Ca^{2+}-free artificial cerebrospinal fluid (ACSF; [in mM] 13.32 NaCal, 0.448 KCl, 10 D-glucose, 1.25 KH_2PO_4, 26 $NaHCO_3$, 2 MgCl) for ~5 min. The brains were then secured to a cutting block by Loctite superglue and the block was placed onto the cutting platform of a Ted Pella Vibratome Series 1000 sectioning system which was also submerged in ice-cold ACSF. Approximately 8-12 slices (400 μm thick) containing visible hippocampus were sectioned from brain. Slices were then hemisected and transferred to a custom tissue warming chamber where they were bathed in oxygenated ACSF containing 2 mM Ca^{2+} and held at 32 °C for at least 1.5 h. At the time of recording, slices were placed in a Warner Instruments RC-22 chamber attached to a Kerr Scientific Tissue Recording System and perfused with oxygenated Ca^{2+} ACSF warmed to ~32 °C using a Cell MicroControls inline HPRE2 preheater and analog TC2BIP temperature controller. Tissue slices were stimulated using a bipolar stimulating electrode placed in stratum radiatum near the CA1 border to activate CA3 Schaffer collaterals, and presynaptic fiber volleys (FVs) and excitatory post-synaptic potentials (EPSPs) were recorded using a recording electrode placed in CA1 stratum radiatum. Stimulus timing and data acquisition were controlled by a Kerr Scientific S2 Amplifier, World Precision Instruments Constant Current Stimulus Isolator, and ADInstruments PowerLab 4/35 acquisition system with LabChart software. Input/output (I/O) curves were generated by stimulating the tissue at 0.033 Hz across a series of predetermined currents (2.5–50 μA) until the maximal EPSP amplitude (mV) was reached for that slice. The stimulating current was then adjusted to elicit a response that was ~33% of the maximal EPSP amplitude for the remainder of the experiment. For measures of paired pulse (PP), slices received two stimuli separated by a series of increasing delay intervals (10–150 ms) in order to obtain two responses: EPSP1 and EPSP2. For long-term potentiation (LTP) measures, EPSPs were recorded at 0.033 Hz for a 20 min baseline period, followed by the delivery of two trains of 100 Hz stimulations (1 s per train, 10 s intertrain interval) to induce LTP. Slices were then recorded at 0.033 Hz for an additional hour. For LTP recordings, the slope of each EPSP was first normalized to the average slope across the 20 min baseline period prior to analysis. LabChart software was used to extract and analyze the following parameters: I/O recordings – population spike (pop spike) threshold, maximal FV amplitude, maximal EPSP amplitude, maximal EPSP slope, and maximal EPSP slope/maximal FV ratio; PP recordings – EPSP1 and EPSP2 amplitudes and PP% increase ([(EPSP1-EPSP2)/EPSP1]*100); LTP recordings – average Baseline EPSP slope, average Early (first 5 min post-100 Hz stim) and Late (last 5 min post-100 Hz stim) LTP slopes (expressed as % of baseline), and average LTP maintenance ([Late LTP % of baseline/Early LTP % of baseline]*100). Values were then averaged across slices within each mouse, resulting in a single data point per animal for each of the parameters.

Statistical analyses: Hippocampal electrophysiology data were screened and analyzed using SPSS 29.0 (IBM Corporation; Armonk, NY). The effect of group (WT Veh, MD Veh, and MD MW150) on Max EPSP Amplitude, Max EPSP Slope, Normalized EPSP, and Pop Spike Threshold were analyzed by linear regression. The interaction between LTP phase (Early LTP vs. Late LTP) and group on LTP maintenance was analyzed by linear regression; a natural log transformation of slope (% of baseline)

resolved the normality of residuals violation for this analysis. Last, the effect of group on Paired Pulse % Increase was analyzed by one-way ANOVA. All figures were generated using GraphPad Prism and Photoshop 2024 (Adobe). Significance was set at $\alpha = 0.05$. All graphs show non-transformed data. The unstandardized B is reported for non-transformed data, and the standardized β for transformed.

3. Results

3.1. Administration of 0.5 mg/kg MW150 preserves MWM performance in MD mice

After 8 weeks of the dietary HHcy induction and MW150 treatment paradigm (Fig. 1), mice discontinued drug and dietary treatments to undergo testing in the MWM. Learning curves are displayed as group means ± SEM for average time to reach the platform by day (Fig. 2a). The main effects of Condition ($F_{(3, 176)} = 4.19$, $p = 0.0068$) and Trial ($F_{(4, 176)} = 36.99$, $p < 0.0001$) were both significant, while the interaction was not ($F_{(12, 176)} = 0.70$, $p = 0.7475$). Compared to the MD Veh condition, the WT Veh (difference (SE) = −8.14 (2.65), $t = 3.07$, $p_{adj} = 0.0070$) and MD 0.5 MW150 groups (difference (SE) = −6.38 (2.65), $t = 2.41$, $p_{adj} = 0.0456$) had significantly reduced latencies. Interestingly, the 2.5 mg/kg dose of MW150 did not rescue the learning deficits in MD mice; there was no difference between the MD Veh and the MD 2.5 MW150 condition (difference (SE) = −1.68 (2.65), $t = 0.63$, $p_{adj} = 0.8631$) (**Supplement 1**). No group differences in sensorimotor or motivational performance were detected in the cued platform trial (Kruskal Wallis $H_{(3)} = 5.542$, $p = 0.136$) (Fig. 2b). No group differences were detected in the probe (1-way ANOVA $F_{(3,44)} = 0.389$, $p = 0.762$) or retention trials (Kruskal Wallis $H_{(3)} = 2.173$, $p = 0.537$) (Fig. 2c and d). Together, these data indicate that the MD saline mice have a modest learning deficit as compared to WT, but no memory deficits in either the 24-h probe nor the 14-week retention trials; findings that are concordant with what has been reported in the 5xFAD model (O'Leary and Brown, 2022). As the 0.5 mg/kg dose but not 2.5 mg/kg dose of MW150 was able to prevent the learning deficits detected in the vehicle-treated MD mice, subsequent experiments were performed with 0.5 mg/kg of MW150.

3.2. Administration of MW150 does not alter amyloid or vascular pathologies

A separate group of mice underwent MRI and terminal brain tissue analyses to identify relevant neuropathological changes affected by MW150 treatment that might underlie the cognitive benefits. Modest hippocampal changes were detectable in MRI measurements between the MD Veh and WT Veh groups: mean diffusivity was significantly increased in the MD Veh group (M = 6.78e-4, SD = 3.46e-5) as compared to WT (M = 6.46e-4, SD = 1.93e-5) ($B = 3.2e-5$, $p = 00.031$), but no effect of MW150 was found ($B = -7.167e-6$, p = 0.6). Although there were significant changes in the MRS-detectable analytes by group in a multiple analysis of variance (MANOVA) test (Wilks' Lambda = 0.086, $F_{(20, 24)} = 2.89$, $p = -0.0073$), the number of analytes was too large relative to our group sizes to reliably interpret individual

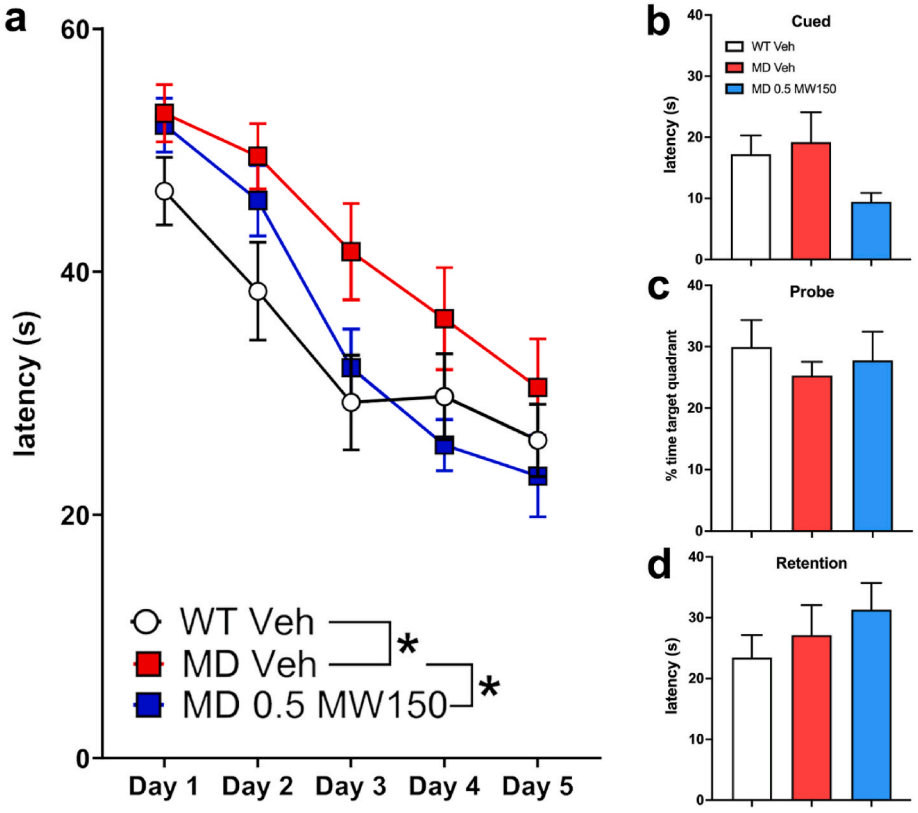

Fig. 2. MW150 prevents behavioral deficits in the Morris Water Maze (MWM) test of hippocampal-dependent spatial learning. (a) Results of MWM acquisition, four trials averaged per day, across the 5 days of testing (n = 12 per group). All groups successfully learned the task, as indicated by decreasing latency to platform measures across the first 4 days of testing. However, the MD Veh mice had higher latencies to reach the platform as compared to WT Veh, suggesting that these animals were cognitively impaired. Administration of MW150 rescued this deficit, but only at a concentration of 0.5 mg/kg. **(b)** No effect of the disease model or drug was detected when a visual cue was placed in the testing arena, indicating that the results shown are not likely due to differences in visual acuity, motor function, or motivational factors between groups. **(c)** In line with the acquisition curve latencies by day 5, there was no difference in time spent in target quadrant between the groups. **(d)** Similarly, assessment of memory retention performed 14 days after the probe trial also showed no differences between groups. See text for statistical details. Data represent means ± SEM. *$p \leq 0.05$.

measures. See **Supplement 1** for full data and for MRS correlational heatmaps.

For more sensitive measures of the neuropathology, we quantified vessel morphology (dystrophin), Aβ deposition (6E10), and microhemorrhages (Prussian blue) in fresh-frozen tissue sections (Fig. 3a). While the overall levels of dystrophin within the HPC (TxRed+ % area) were not altered by either the model or the drug (Fig. 3b; 1-way ANOVA $F_{(2,29)} = 0.1211$, $p = 0.8864$), HPC vessel density (number of TxRed+ objects normalized to HPC area) was slightly increased in both MD groups compared to WT, though this did not reach significance (1-way ANOVA $F_{(2,29)} = 3.193$, $p = 0.0558$; Sidak's post-hoc WT Veh vs. MD Veh $p = 0.0717$). Analysis of 6E10 staining (FITC) revealed similar results, with MW150 administration having no effect on either Aβ plaque number (Student's *t*-Test $t_{(23)} = 0.4331$, $p = 0.6690$) or plaque size (Student's *t*-Test $t_{(23)} = 0.4099$, $p = 0.6857$) within the HPC. To further confirm these findings, we quantified the degree of cerebral amyloid angiopathy (CAA) (% area of colocalized TxRed and FITC signal) and number of microhemorrhages (Prussian blue+ objects normalized to HPC area). No effect of MW150 was detected on the amount of CAA in the MD mice (Fig. 3c). Analysis of whole tissue sections revealed that while the MD mice had significantly more microhemorrhages vs. WT Veh (Fig. 3d; 1-way ANOVA $F_{(2,33)} = 8.011$, $p = 0.0015$; Sidak's pos-hoc WT Veh vs. MD Veh $p = 0.0184$), MW150 did not significantly alter this pathology.

3.3. Administration of MW150 does not reduce neuroinflammation

The inhibition of p38α has previously been shown to attenuate neuroinflammation in AD mice, so we measured the levels of proinflammatory cytokines in the HPC using MSD ELISA (Fig. 4a). Multiple analysis of variance (MANOVA) was used to determine the omnibus effect of group conditions across all 11 proinflammatory cytokines and further multivariate general linear model (GLM) analysis was used to determine the univariate effects of group condition on each of the cytokines. There was a group effect across all cytokines, (Wilks' Lambda = 0.10, $F_{(22,\ 36)} = 3.43$, $p < 0.001$) where, as expected, MD Veh mice had significant elevations in several cytokines compared to WT animals: IL-1β, KC/GRO, TNFα, MCP-1, IL-27p28/IL-30, MIP-1α, MIP-2, and IP-10. The MD mice treated with MW150 also showed a similar pattern of increased expression, and no differences were detected between MD Veh and MD 0.5 MW150 groups, indicating that the drug did not attenuate proinflammatory cytokine levels at this dosage or timepoint.

To determine if p38α suppression reduced the activation of astrocytes or microglia, we quantified the amount of GFAP (Fig. 4b) and IBA1 (Fig. 4c) in HPC tissue sections. No differences were detected in the total number of HPC astrocytes across groups; however, both MD groups had significant elevations in astrocyte size (Kruskal-Wallis test $K–W = 8.099$, $p = 0.0174$; Dunn's post-hoc WT Veh vs. MD Veh $p = 0.0369$),

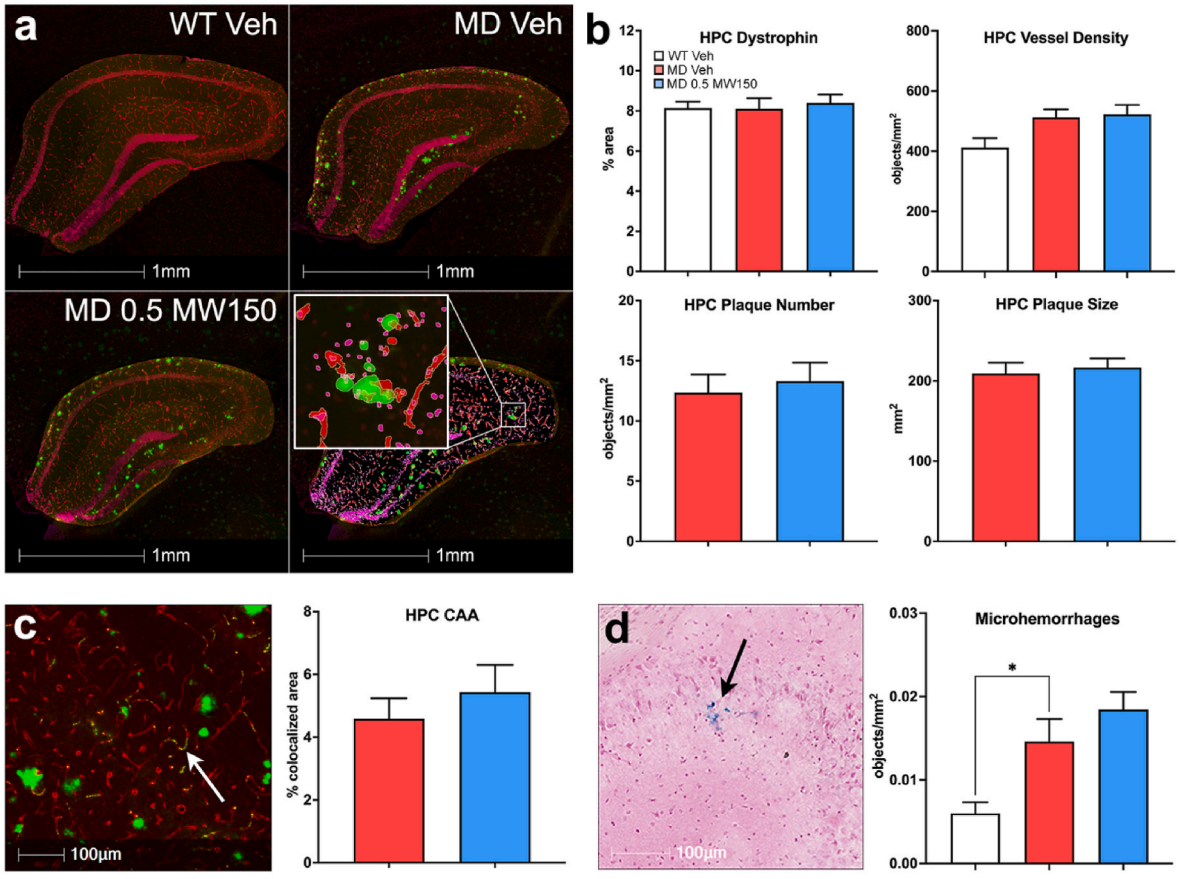

Fig. 3. Measures of amyloid and vascular pathology in the HPC. (a) Representative tissue sections from WT and MD mice (n = 7–13 per group) after IF staining. The dorsal HPC region analyzed is highlighted in each image for display purposes. The output of the quantification algorithm is shown in the bottom right panel. Zoomed in images of ROIs representing vessels (red), Aβ plaques (green), and nuclei (purple) are shown in the inset. **(b)** Dystrophin staining and vessel density, plaque number, and plaque size did not differ across any of the groups **(c)** Representative image of cerebral amyloid angiopathy (CAA) in the HPC. White arrow points to a vessel (red) containing deposits of 6E10 amyloid (green objects). The total amount of CAA in the MD mice was unchanged by treatment with MW150. **(d)** An image of a tissue section after Prussian blue (PB) staining. Microhemorrhages were defined as spots of diffuse blue color (black arrow) that corresponded to regions of iron deposition. Microhemorrhage numbers across the entire section were first quantified in HALO software using the classifier utility, then visually confirmed by two independent, blinded investigators. Results indicated that both MD Veh and MD 0.5 MW150 mice had significantly more microhemorrhages compared to WT Veh, but no effect of MW150 was detected ($p > 0.05$). Data represent means ± SEM. *$p \leq 0.05$. See text for statistical details. (For interpretation of the references to color in this figure legend, the reader is referred to the Web version of this article.)

suggesting astrocyte activation and hypertrophy in these animals. Similarly, the total number of microglia (Brown-Forsyth ANOVA $F_{(2,23.76)} = 10.02, p = 0.0007$; Dunnett's T3 post-hoc WT Veh vs. MD Veh $p = 0.0002$) as well as the number of activated microglia (Brown-Forsyth ANOVA $F_{(2,22.48)} = 7.041, p = 0.0042$; Dunnett's T3 post-hoc WT Veh vs. MD Veh $p = 0.0013$) were significantly elevated in MD mice. As with the measures of proinflammatory cytokines, MW150 did not attenuate glial cell activation in these animals (all associated post-hocs of MD Veh vs.

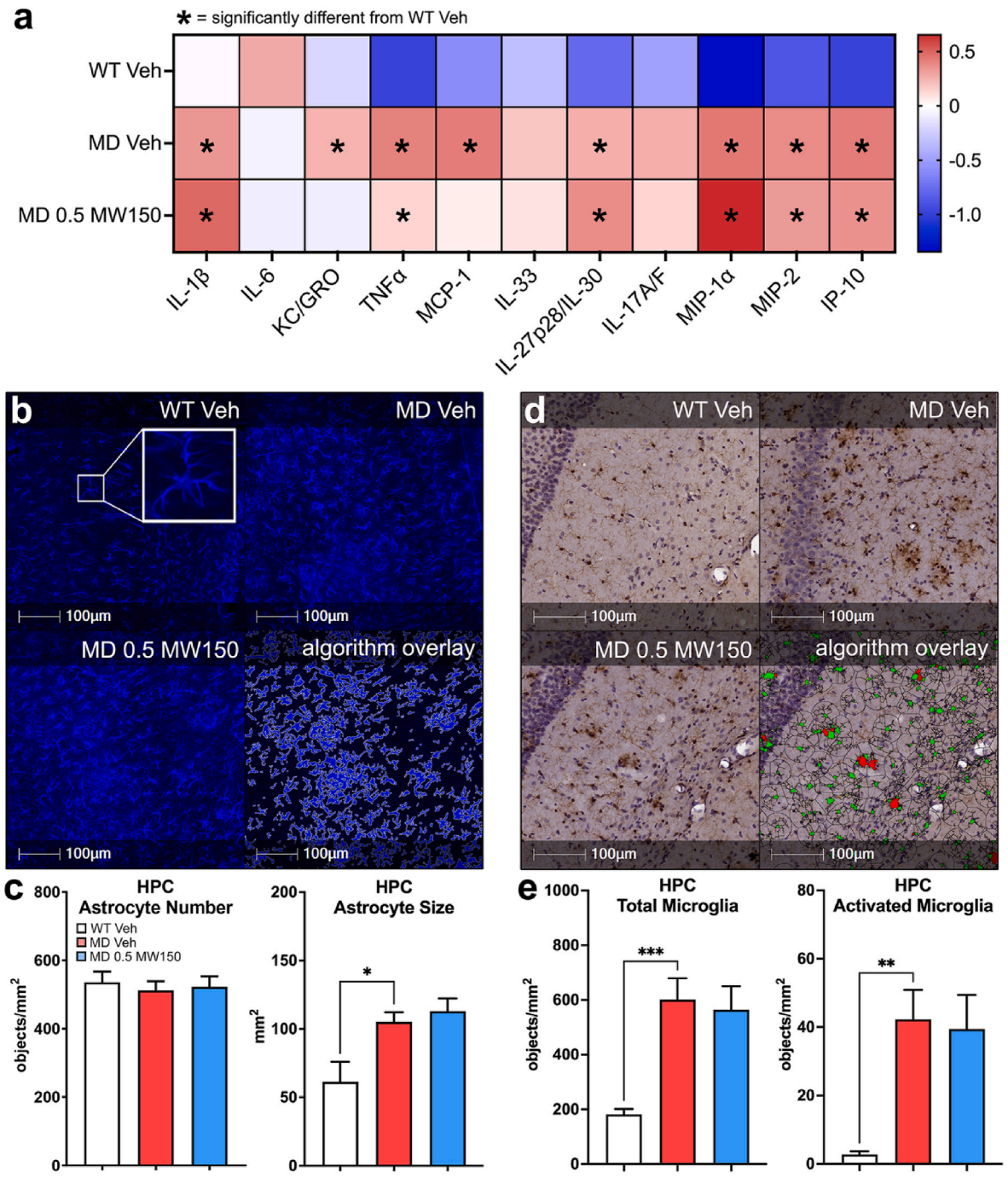

Fig. 4. Assessment of neuroinflammation in WT and MD mice. (a) Proinflammatory cytokine levels in the HPC were measured using MSD ELISA (n = 11–13 mice per group). Normalized cytokine concentrations ([pg/mL]/mg) underwent a Z-score transformation and are displayed as a heatmap across the groups. *p < 00.05 versus WT Veh group. Of the cytokines significantly elevated in the MD Veh group, none were significantly reduced by treatment with MW150; however, KC/GRO and MCP-1 were no longer significantly different from the WT Veh group. **(b)** Representative images of GFAP staining in the HPC of WT and MD mice (n = 7–11 per group). Upper left inset shows an individual astrocyte with non-reactive morphology. Bottom right image shows the output of the HALO analysis algorithm. **(c)** Quantification showed no differences in the total number of astrocytes (GFAP+ objects) between groups; however, MD Veh mice had significantly larger GFAP+ astrocyte sizes compared to WT Veh, corresponding to enhanced astrocyte activation and hypertrophy. Neither measure was reduced by MW150. **(d)** Representative images of sections stained for IBA1 (n = 7–11 mice per group). Bottom right image shows the MD 0.5 MW150 section after analysis using HALO microglial activation analysis module. **(e)** Quantification revealed that compared to WT, MD Veh mice had greater overall numbers of HPC microglia as well as significantly more microglia with an activated phenotype. As with measures of astrocytes, MW150 did not reduce total microglial numbers or the amount of activated microglia. Data represent means ± SEM. *$p \leq 0.05$; **$p \leq 0.01$; ***$p \leq 0.001$. See text for additional statistical details.

MD 0.5 MW150 $p > 0.05$). Together, these findings indicate that the beneficial effects of MW150 in this paradigm may be due to changes in neuronal health or physiology rather than glial as expected; we therefore next assessed whether there were differences in synapse number or tau protein levels.

3.4. Functional effects of MW150 administration are associated with restored HPC synaptic protein levels and reduced phosphorylation of tau at Thr231

To determine if these beneficial changes in neuronal function were associated with changes in synaptic morphology, we quantified the levels of two synaptic proteins (synaptophysin and PSD95) using IF and confocal microscopy (n = 8–13 per group) (Fig. 5a). Compared to WT, MD Veh animals had significant decreases in the levels of both synaptophysin (Brown-Forsyth ANOVA $F_{(2,23.49)} = 9.843$, $p = 0.0008$; Dunnett's T3 post-hoc WT Veh vs. MD Veh $p = 0.0073$) and PSD95 (1-way ANOVA $F_{(2,28)} = 7.133$, $p = 0.0031$; Sidak's post-hoc WT Veh vs. MD Veh $p = 0.0030$) in HPC area CA1 (Fig. 5b). Administration of MW150 completely restored both proteins back to WT Veh levels (post-hocs of MD Veh vs. MD 0.5 MW150 $p = 0.0017$ and $p = 0.0122$, respectively). This same effect was also detected in area CA3 ([Brown-Forsyth ANOVA of synaptophysin $F_{(2,18.19)} = 5.324$, $p = 0.0151$], [Brown-Forsyth ANOVA of PSD95 $F_{(2,20.84)} = 18.93$, $p < 0.0001$]) suggesting the drug could alter synaptic protein expression throughout the HPC (Fig. 5c). As synaptophysin is predominantly presynaptic while PSD95 is preferentially expressed post-synaptically, we also quantified the number of colocalized synaptophysin+ and PSD95+ objects as a measure of overall synapse density. MD Veh mice had reduced synapse numbers in both CA1 (Brown-Forsyth ANOVA $F_{(2,\ 13.45)} = 5.967$, $p = 0.0140$; Dunnett's T3 post-hoc WT Veh vs. MD Veh $p = 0.0268$) and CA3 (Brown-Forsyth ANOVA $F_{(2,12.19)} = 6.234$, $p = 0.0136$; Dunnett's T3 post-hoc WT Veh vs. MD Veh $p = 0.0273$) compared to WT (Fig. 5b and c). As with measures of synaptophysin and PSD95 alone, MW150 completely restored synapse density back to WT Veh levels (post-hocs of MD Veh vs. MW150 $p = 0.0187$ and $p = 0.0063$, respectively).

As aberrant tau phosphorylation has been implicated in improper trafficking of synaptic components (Hoover et al., 2010; Jurado, 2017), and p38 inhibition has been reported to reduce this in some AD models (Maphis et al., 2016), we quantified the levels of total and

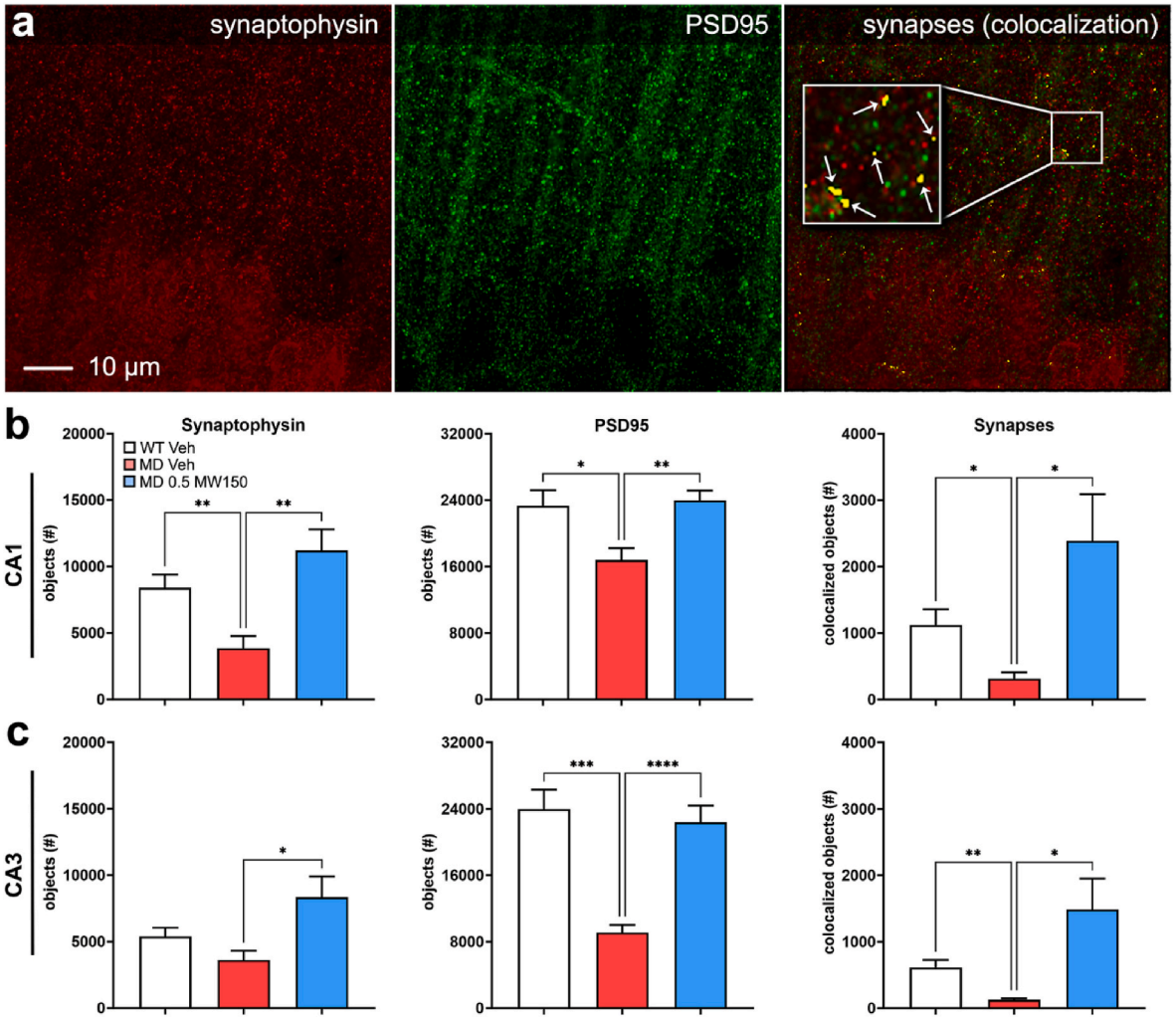

Fig. 5. Quantification of synaptic proteins in the HPC of WT and MD mice. (a) Pseudo-colored images of WT Veh tissue stained for synaptophysin (red) and PSD95 (green) in HPC areas CA1 and CA3 (1 image per area, 1 section per mouse, n = 9–13 mice per group) are shown. Synapses (right image) were defined as synaptophysin+ and PSD95+ puncta directly colocalized with one another within the 3D plane. White arrows in inset point to objects (yellow dots) positively identified as colocalized puncta by the analysis software. **(b)** Quantification revealed that compared to WT, MD Veh mice had a significant decrease in CA1 levels of both synaptophysin and PSD95, as well as a reduction in the number of CA1 synapses. **(c)** Similar effects were detected in area CA3. MW150 administration ameliorated the loss of synaptic proteins in both HPC areas, with MD 0.5 MW150 animals having numbers comparable to WT Veh ($p > 0.05$, respectively). Data represent means ± SEM. *$p < 0.05$; **$p < 0.01$; ***$p < 0.001$; ****$p < 0.0001$. See text for additional statistical details. (For interpretation of the references to color in this figure legend, the reader is referred to the Web version of this article.)

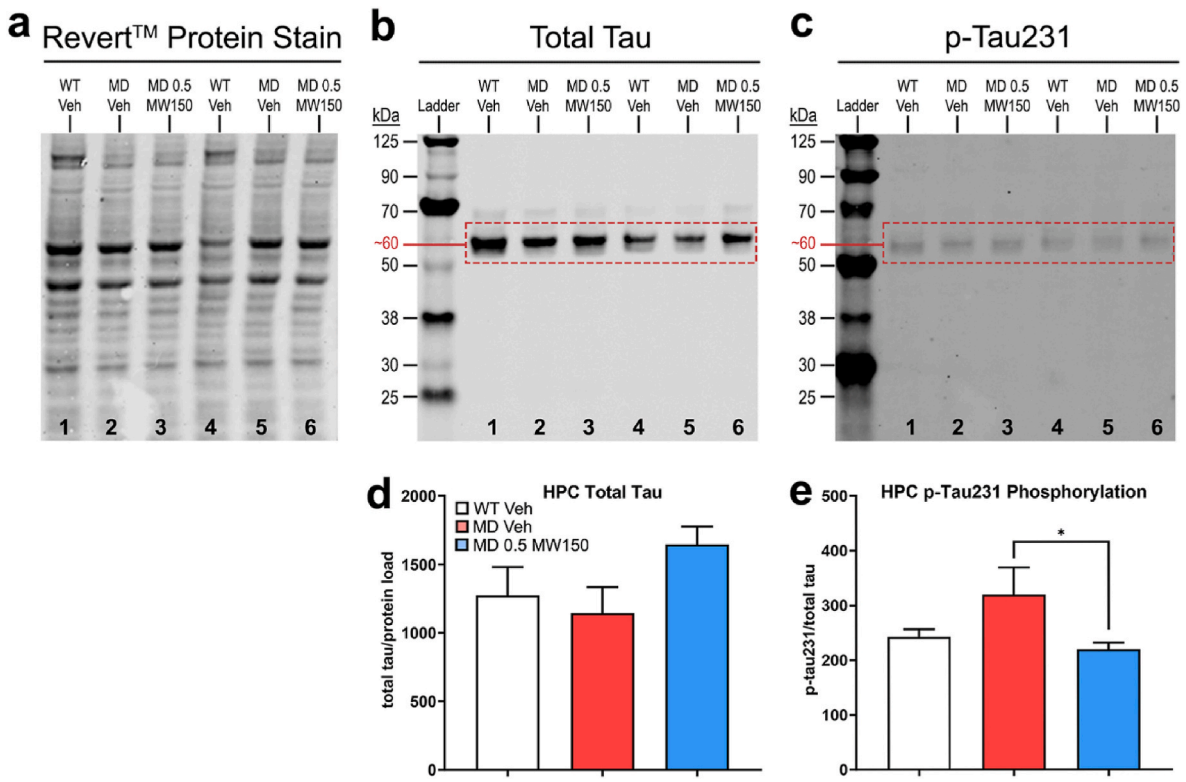

Fig. 6. Assessment of HPC tau phosphorylation. (a–c) Representative images of Western immunoblots performed on homogenized HPC tissue from WT and MD mice (n = 7–8 per group). Blots were normalized to total protein across the lane, rather than a housekeeping protein, and probed for total tau and Thr231 phosphorylated tau (p-tau231). All statistical analyses were performed on raw fluorescent imaging files using Li-Cor Empiria Studio® analysis software. For display purposes, representative images are presented in grayscale with adjusted brightness/contrast levels. **(d)** Quantification of overall tau levels in the HPC using a linear regression analysis showed no differences between groups. **(e)** To determine the degree of tau phosphorylation, raw p-tau231 values were normalized to raw total tau values in order to generate p-tau231/total tau ratios. A linear regression analysis performed on natural log (ln) p-tau231/total tau ratio revealed that tau phosphorylation was marginally but non-significantly increased in the HPC of MD Veh mice compared to WT. This slight elevation was attenuated by MW150 administration, with MD 0.5 MW150 mice having decreased ratios compared to MD Veh. Data represent means ± SEM. *$p \leq 0.05$; **$p \leq 0.01$; ***$p \leq 0.001$; ****$p \leq 0.0001$. See text for additional statistical details.

phosphorylated Thr231 tau (p-tau231) in homogenized HPC samples from WT and MD mice (n = 8 per group) (Fig. 6). Comparison of total tau protein levels using a linear regression analysis indicated no differences between groups (Fig. 6d). However, analysis of tau phosphorylation at Thr231 relative to total tau (p-tau231/total tau) indicated that MD Veh mice had marginally elevated ratios compared to WT Veh (Fig. 6e; $\beta = -0.39$, $p = 0.09$). Interestingly, this increase in p-tau231/total tau ratios arising from the MD manipulation was significantly blunted in the MD 0.5 MW150 group ($\beta = -0.57$, $p < 0.05$), suggesting that p38α inhibition may also prevent Thr231 hyperphosphorylation of tau, thereby contributing to the integrity of synaptic function.

3.5. Administration of MW150 normalizes synaptic transmission in HPC neurons

To determine the effect of p38α inhibition on synaptic transmission in the HPC, we performed extracellular field recordings in acute brain slices from WT and MD mice (n = 8–9 per group). Mice first underwent testing of working/spatial reference memory in the NSR, but none of the groups showed impairment on this task (**Supplement 1**). Subsequently, I/O recordings taken in HPC area CA1 were used to derive measures of basal synaptic strength: maximum EPSP amplitude, maximum EPSP slope, and normalized EPSP slope (slope/FV) (Fig. 7a and b). No differences were detected between groups for any of these measures, suggesting that neither the model nor MW150 significantly altered basal strength in this area. However, quantification of the minimum stimulation required to generate a population spike (pop spike threshold) revealed that MD Veh mice generated pop spikes at significantly lower levels of stimulation compared to WT Veh ($B = -5.90$, $p < 0.01$), suggesting increased neuronal excitability in these animals. Interestingly, administration of MW150 significantly elevated pop spike thresholds in MD mice compared to vehicle ($B = 6.32$, $p < 0.01$), implying p38α inhibition may attenuate hyperexcitability associated with mixed AD/vascular pathologies.

We also performed LTP recordings (Fig. 7c) to determine if p38α inhibition improves the induction or maintenance of synaptic potentiation following a 100 Hz stimulation. There was no change in the potentiation amplitude; however, analysis of EPSP slopes during the Early (first 5 min post-induction) and Late (last 5 min post-induction) phases of the recording revealed that MD Veh mice could not maintain the initial increase in EPSP response ($\beta = -0.761$, $p < 00.001$), with Late LTP slopes fully returning to baseline values by the end of the recording (Fig. 7d). Conversely, neither WT Veh ($\beta = -0.110$, $p > 0.05$) nor MD 0.5 MW150 ($\beta = -0.156$, $p > 0.05$) mice demonstrated differences in EPSP response between the Early and Late phases of the recording, suggesting a complete maintenance of LTP in these animals.

Finally, a hyperexcitable effect was also detected when analyzing the % increase between the first and second EPSP responses recorded during the PP protocol (Fig. 7e). Using a multilevel linear mixed effects model, we first compared the rate of change in PP% increase (slope) across a series of delays (10–150 ms) and saw no interaction effects between delay period and groups. We therefore collapsed the PP% increase values across delays and performed a comparison of group means using a 1-way ANOVA. Results indicated that MD Veh mice had a significantly greater average % increase compared to WT Veh animals, again suggesting this tissue was hyperexcitable ($F_{(2,24)} = 17.11$, $p < 0.0001$;

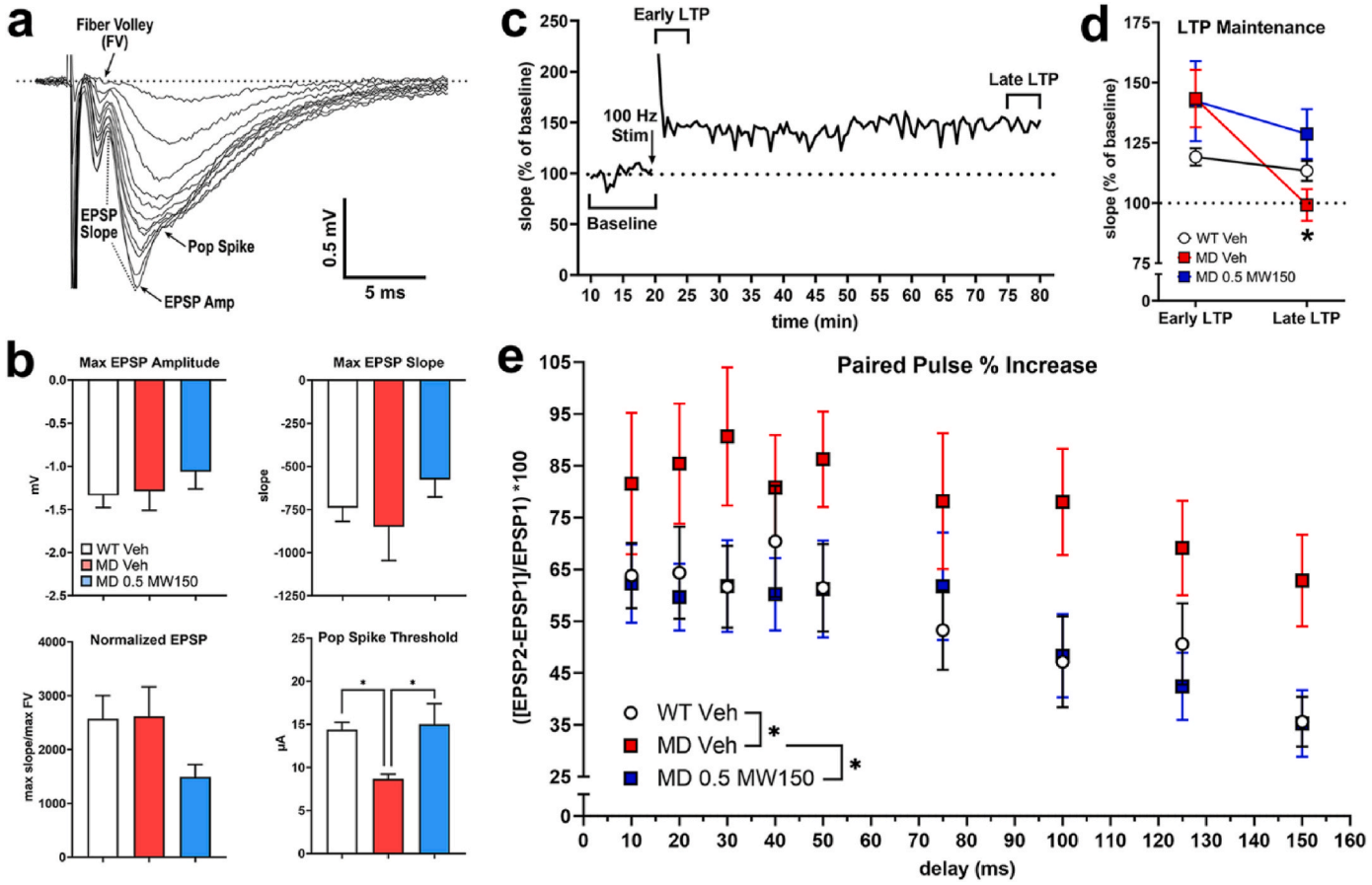

Fig. 7. Electrophysiological assessment of HPC synaptic function in WT and MD mice. Extracellular field recordings were performed in acute brain slices (n = 1–4 slices per mouse, 8–10 mice per group) by stimulating the Schaffer collaterals of HPC area CA3 and recording from area CA1 to quantify basal synaptic strength (input/output [I/O] recordings), short-term plasticity (paired pulse [PP] recordings), and long-term plasticity (long-term potentiation [LTP] recordings). **(a)** Representative traces from an I/O recording in a WT Veh slice. Labels indicate fiber volley amplitudes (FV), EPSP amplitudes (EPSP Amp) and slopes (EPSP Slope), and the level of stimulating current (μA) at which the first population spike (Pop Spike) was generated. **(b)** Quantification of I/O recordings showed no differences in Max EPSP Amplitudes, Max EPSP Slopes, or Normalized EPSP Slopes (defined as max slope/max FV) across groups. However, the stimulating current at which a pop spike was first generated (Pop Spike Threshold) was lower in slices from MD Veh mice compared to WT Veh ($B = -5.903$, $p < 0.01$), suggesting hyperexcitability. Treatment with MW150 significantly raised the Pop Spike Thresholds compared to MD Veh, ($B = 6.319$, $p < 00.01$). **(c)** A representative trace from an LTP recording performed in a WT Veh slice indicating the definition of Early LTP (first 5 min post-induction) versus Late LTP (last 5 min post-induction). All EPSP slopes were normalized to the average baseline slope value and expressed as % of baseline. **(d)** Linear regression indicated that LTP maintenance significantly decreased from Early to Late LTP for slices in the MD Veh group ($\beta = -0.761$, $p < 00.001$) but was unchanged in the MD 0.5 MW150 ($\beta = -0.156$, n. s.) and WT Veh ($\beta = -0.110$, n. s.) groups. **(e)** To determine the effect of p38α inhibition on short term plasticity, a PP protocol comprised of 2 stimulations separated by a series of increasing delays (10–150 ms intervals) was used to generate 2 EPSP responses: EPSP1 and EPSP2. Analysis of the average PP% increase across all delays, indicated that MD Veh mice had a significantly greater mean increase compared to WT Veh, further suggesting hyperexcitability in these animals. This effect was attenuated by MW150 (MD Veh vs. MD 0.5 MW150 $p < 0.0001$). Data represent means ± SEM. $^{*}p \leq 0.05$; $^{***}p \leq 0.001$. See text for additional statistical details.

Sidak's post-hoc WT Veh vs. MD Veh $p = 0.0001$). As with pop spike measures, the PP% increase was attenuated by MW150 (MD Veh vs. MD 0.5 MW150 $p < 0.0001$). Taken together, these measures indicate that inhibition of p38α can reduce neuronal hyperexcitability as well as improve LTP maintenance in the context of mixed AD and vascular pathology.

4. Discussion

We report here the effects of therapeutic administration of a highly specific, small molecule p38α inhibitor drug candidate, MW150, in a preclinical model of comorbid amyloid and vascular pathology. We began with a study designed around the outcome of hippocampal-dependent MWM performance, and subsequently worked to identify the underlying physiological changes associated with neuroprotection. It is important to note that the present study reports only female mice because age-matched male mice failed to show impairments in the MWM at this age. This is likely due to some combination of slower progressing amyloid pathology (Sil et al., 2022) and resistance to the HHcy pathology (Braun et al., 2019). Future studies utilizing male mice with more advanced pathology will be important to determine what impact, if any, sex has on p38α inhibition in this context. Nonetheless, we confirmed the presence of vascular (CAA, microhemorrhage) and Aβ neuropathologies in the MD model mice, with associated elevations in glial activation and proinflammatory cytokine levels, impaired neuronal function, and worsened behavioral performance compared to WT controls. Interestingly we found that MW150 prevented MWM impairment in the MD mice, associated with a normalization of neuronal function and synaptic morphology, but no effects on Aβ, vascular, or neuroinflammatory measurements. Overall, our data suggest that, at least in certain contexts, the major functional benefit of small molecule p38α inhibition may be attributable primarily to neuronal changes. These findings emphasize the importance of future studies to define the relevant p38α-driven neuronal signaling pathways and to elucidate cell-specific and disease-specific roles of p38α.

Although we found the 2.5 mg/kg dose of MW150 efficacious in

other models (Roy et al., 2015), it is interesting that only the 0.5 mg/kg dose provided functional benefit in the MWM in the mixed pathology context. There are several mutually inclusive possibilities that may underlie these findings. First, the severe restriction of several metabolically important B vitamins (B_6, B_9, B_{12}) required to induce HHcy may affect the pharmacokinetic/pharmacodynamic properties of MW150 and therefore effective dosing strategy. Second, HHcy is associated with oxidative damage (Obeid and Herrmann, 2006) and p38α activation at lower levels is known to trigger protective responses to this type of stressor (Canovas and Nebreda, 2021). The higher dose of MW150 may therefore attenuate not only the harmful consequences of p38α over-activation, but also the protective effects of more moderate activation. Finally, it is important to note that the behavioral deficits in this model are more representative of an early stage of cognitive impairment. The MD Veh group still managed to achieve WT performance by day 5 of testing, albeit somewhat more slowly, as indicated by decreased latencies during MWM acquisition phase but no difference in the probe or retention trials. Additionally, the MD mice were not impaired in the NSR task (**Supplement 1**). It may be the case that the p38α-associated neuroinflammatory changes at this early neuropathological stage are on balance neuroprotective (Ennerfelt and Lukens, 2020), and the higher MW150 dose achieves deleterious anti-inflammatory effects that override the beneficial neuronal ones. Indeed, we have previously shown that the 2.5 mg/kg dose reduces cytokine levels in older APP/PS1 mice with more advanced pathology, and in that context it is associated with an improvement in water maze performance (Zhou et al., 2017). Additionally, p38α has been reported to activate anti-inflammatory pathways and promote the release of anti-inflammatory cytokines such as IL-10, as well as regulate the activation of other immune cells, such as macrophages (Canovas and Nebreda, 2021; Raza et al., 2017). The precise timing and context are therefore crucial for p38α inhibition to provide therapeutic benefit, and while we did not explore the null effect of the 2.5 mg/kg dose, future studies parsing these mechanisms in more clinically relevant models of mixed disease are vital to inform future clinical studies. For example, the use of an aged "AD risk" mouse model (Baglietto-Vargas et al., 2021) with a more clinically-relevant contributor to vascular pathology (e.g. high fat diet), may help to answer these important and timely questions.

Nonetheless, while MW150 successfully prevented hippocampal-dependent spatial learning deficits in the MWM, we found little effect on our primary outcome measures relating to amyloid pathology, vascular pathology, and neuroinflammation. Consistent with our prior studies using pharmacological inhibitors of p38α (Zhou et al., 2017), we found no differences in number or size of amyloid plaques. Similarly, although the inhibition of p38 has been reported to protect against certain types of cerebrovascular injury such as stroke (Hou et al., 2022; Barone et al., 2001), we found no change in vessel morphology, CAA, or microhemorrhages with MW150 treatment. Surprisingly, the neuroinflammatory phenotype in the MD mice was unchanged by MW150; however, we found significant drug effects on neuronal endpoints that may contribute to the behavioral rescue. First, MW150 treatment restored both the levels of synaptophysin and PSD95 as well as the number of HPC synapses back to WT levels. Further, given that p38α can phosphorylate tau at multiple sites such as Thr231, and tau phosphorylation can affect synaptic integrity (Wu et al., 2021), we measured tau phosphorylation at Thr231. The p-tau231/total tau ratios were significantly decreased with MW150 administration, raising the possibility that MW150 may alter the balance between phosphorylated and non-phosphorylated tau species. These data are consistent with our previous study with an earlier generation p38α inhibitor demonstrating reductions in tau phosphorylation in a tauopathy model (Maphis et al., 2016). Notably, another p38α inhibitor, Neflamapimod, has also been reported to rescue behavioral deficits in rodents when administered at a dose lower than the one required to reduce hippocampal cytokine levels (Alam, 2015), indicating important dose-dependencies in cellular targeting with this general class of compounds.

Electrophysiological assessment in HPC area CA3-CA1 neurons indicated that MD model mice had a hyperexcitable phenotype, represented by reductions in pop spike thresholds and greater PP% increases, consistent with well-documented hyperexcitability in the HPC of AD mice (Targa Dias Anastacio et al., 2022). MW150 treatment completely rescued these hyperexcitable synaptic changes, resulting in pop spike thresholds and PP% increases comparable to those found in WT mice. Importantly, we also showed that inhibiting p38α in MD mice improved LTP maintenance, an important component in the consolidation of long-term memory. LTP maintenance is controlled in part by the trafficking of AMPA receptors (AMPAR). Specifically, preserving postsynaptic AMPAR levels by inhibiting their endocytosis is associated with improved LTP maintenance (Dong et al., 2015). Prior work has reported that p38α can mediate glutamate transmission by altering the expression of glutamate receptors in postsynaptic neurons (Asih et al., 2020), and p38 activation has been shown to accelerate the loss of AMPAR at synapses (Huang et al., 2004). Thus, it could be that inhibition of p38α restored glutamatergic signaling to homeostatic levels thereby rescuing LTP maintenance in MD mice here. Alternatively (or additionally), inhibition of p38α may have maintained synaptic plasticity via a restoration of synaptic density.

5. Conclusions

Taken together, our work suggests that the behavioral benefits associated with p38α inhibition in this study are due primarily to improved synaptic function and a reduction in neuron-specific pathology. The downstream molecular mechanisms driving these effects, such as which receptors, ion channels, and/or transcriptional pathways are altered in response to p38α activation, are still unknown. Future investigations focused on elucidating the cell-specific roles of p38α in this and other models of mixed pathology are needed in order to further refine the development of p38α inhibitors in the clinic and potentially open new therapeutic avenues.

Availability of data and materials

The datasets supporting the conclusions of this article are included entirely within the article and its additional supplemental files.

Funding

This work was supported by National Institute on Aging (NIA) Training Grants T32AG057461 (HNF) and T32AG078110 (CSB), RF1AG064859 (LVE), and U01AG043415 (SMR). The funders had no role in study design, data collection and analysis, decision to publish, or preparation of the manuscript.

CRediT authorship contribution statement

Hilaree N. Frazier: Formal analysis, Investigation, Methodology, Writing – original draft, Writing – review & editing. **David J. Braun:** Conceptualization, Data curation, Investigation, Methodology, Supervision, Writing – original draft, Writing – review & editing. **Caleb S. Bailey:** Data curation, Formal analysis, Investigation, Methodology, Writing – review & editing. **Meggie J. Coleman:** Data curation, Investigation, Methodology, Writing – review & editing. **Verda A. Davis:** Investigation, Methodology, Writing – review & editing. **Stephen R. Dundon:** Investigation, Methodology, Writing – review & editing. **Christopher J. McLouth:** Data curation, Formal analysis, Writing – review & editing. **Hana C. Muzyk:** Investigation, Writing – review & editing. **David K. Powell:** Data curation, Methodology, Writing – review & editing. **Colin B. Rogers:** Methodology, Software, Writing – review & editing. **Saktimayee M. Roy:** Resources, Writing – review & editing. **Linda J. Van Eldik:** Conceptualization, Funding acquisition, Project administration, Writing – review & editing.

Declaration of competing interest

The authors declare that they have no known competing financial interests or personal relationships that could have appeared to influence the work reported in this paper.

Data availability

The full dataset is included in Supplement 1.

Acknowledgements

We thank Dr. Chris Gant for providing training and technical assistance during electrophysiology experiments. All MWM behavioral data were obtained by personnel at The Jackson Laboratory. Other behavioral data (NSR) were obtained at the University of Kentucky with the assistance of the Sanders-Brown Mouse Behavioral Facility. We thank the staff at the University of Kentucky Division of Laboratory Animal Research (DLAR) for providing high-quality care and husbandry to all animals included in the study.

Appendix A. Supplementary data

Supplementary data to this article can be found online at https://doi.org/10.1016/j.bbih.2024.100826.

References

Alam, J.J., 2015. Selective brain-targeted antagonism of p38 MAPKalpha reduces hippocampal IL-1beta levels and improves Morris water maze performance in aged rats. J Alzheimers Dis 48 (1), 219–227.
Andreasson, K.I., Bachstetter, A.D., Colonna, M., Ginhoux, F., Holmes, C., Lamb, B., et al., 2016. Targeting innate immunity for neurodegenerative disorders of the central nervous system. J. Neurochem. 138 (5), 653–693.
Asih, P.R., Prikas, E., Stefanoska, K., Tan, A.R.P., Ahel, H.I., Ittner, A., 2020. Functions of p38 MAP kinases in the central nervous system. Front. Mol. Neurosci. 13, 570586.
Bachstetter, A.D., Van Eldik, L.J., 2010. The p38 MAP kinase family as regulators of proinflammatory cytokine production in degenerative diseases of the CNS. Aging Dis 1 (3), 199–211.
Bachstetter, A.D., Xing, B., de Almeida, L., Dimayuga, E.R., Watterson, D.M., Van Eldik, L.J., 2011. Microglial p38alpha MAPK is a key regulator of proinflammatory cytokine up-regulation induced by toll-like receptor (TLR) ligands or beta-amyloid (Abeta). J. Neuroinflammation 8, 79.
Baglietto-Vargas, D., Forner, S., Cai, L., Martini, A.C., Trujillo-Estrada, L., Swarup, V., et al., 2021. Generation of a humanized Abeta expressing mouse demonstrating aspects of Alzheimer's disease-like pathology. Nat. Commun. 12 (1), 2421.
Barone, F.C., Irving, E.A., Ray, A.M., Lee, J.C., Kassis, S., Kumar, S., et al., 2001. Inhibition of p38 mitogen-activated protein kinase provides neuroprotection in cerebral focal ischemia. Med. Res. Rev. 21 (2), 129–145.
Braun, D.J., Abner, E., Bakshi, V., Goulding, D.S., Grau, E.M., Lin, A.L., et al., 2019. Blood flow deficits and cerebrovascular changes in a dietary model of hyperhomocysteinemia. ASN Neuro 11, 1759091419865788.
Braun, D.J., Powell, D.K., McLouth, C.J., Roy, S.M., Watterson, D.M., Van Eldik, L.J., 2022. Therapeutic treatment with the anti-inflammatory drug candidate MW151 may partially reduce memory impairment and normalizes hippocampal metabolic markers in a mouse model of comorbid amyloid and vascular pathology. PLoS One 17 (1), e0262474.
Braun, D.J., Frazier, H.N., Davis, V.A., Coleman, M.J., Rogers, C.B., Van Eldik, L.J., 2023. Early chronic suppression of microglial p38alpha in a model of Alzheimer's disease does not significantly alter amyloid-associated neuropathology. PLoS One 18 (5), e0286495.
Canovas, B., Nebreda, A.R., 2021. Diversity and versatility of p38 kinase signalling in health and disease. Nat. Rev. Mol. Cell Biol. 22 (5), 346–366.
Dong, Z., Han, H., Li, H., Bai, Y., Wang, W., Tu, M., et al., 2015. Long-term potentiation decay and memory loss are mediated by AMPAR endocytosis. J. Clin. Invest. 125 (1), 234–247.
Dunn, O.J., 1961. Multiple comparisons among means. J. Am. Stat. Assoc. 56 (293), 52.
Dunnett, C.W.A., 1955. Multiple comparison procedure for comparing several treatments with a control. J. Am. Stat. Assoc. 50 (272), 1096–1121.
Ennerfelt, H.E., Lukens, J.R., 2020. The role of innate immunity in Alzheimer's disease. Immunol. Rev. 297 (1), 225–246.
Grammas, P., 2011. Neurovascular dysfunction, inflammation and endothelial activation: implications for the pathogenesis of Alzheimer's disease. J. Neuroinflammation 8, 26.
Heneka, M.T., Carson, M.J., El Khoury, J., Landreth, G.E., Brosseron, F., Feinstein, D.L., et al., 2015. Neuroinflammation in Alzheimer's disease. Lancet Neurol. 14 (4), 388–405.
Heppner, F.L., Ransohoff, R.M., Becher, B., 2015. Immune attack: the role of inflammation in Alzheimer disease. Nat. Rev. Neurosci. 16 (6), 358–372.
Hoover, B.R., Reed, M.N., Su, J., Penrod, R.D., Kotilinek, L.A., Grant, M.K., et al., 2010. Tau mislocalization to dendritic spines mediates synaptic dysfunction independently of neurodegeneration. Neuron 68 (6), 1067–1081.
Hou, K., Xiao, Z.C., Dai, H.L., 2022. p38 MAPK endogenous inhibition improves neurological deficits in global cerebral ischemia/reperfusion mice. Neural Plast. 2022, 3300327.
Huang, C.C., You, J.L., Wu, M.Y., Hsu, K.S., 2004. Rap1-induced p38 mitogen-activated protein kinase activation facilitates AMPA receptor trafficking via the GDI.Rab5 complex. Potential role in (S)-3,5-dihydroxyphenylglycene-induced long term depression. J. Biol. Chem. 279 (13), 12286–12292.
Jurado, S., 2017. AMPA receptor trafficking in natural and pathological aging. Front. Mol. Neurosci. 10, 446.
Kapasi, A., Schneider, J.A., 2016. Vascular contributions to cognitive impairment, clinical Alzheimer's disease, and dementia in older persons. Biochim. Biophys. Acta 1862 (5), 878–886.
Lenart, N., Brough, D., Denes, A., 2016. Inflammasomes link vascular disease with neuroinflammation and brain disorders. J Cereb Blood Flow Metab 36 (10), 1668–1685.
Maphis, N., Jiang, S., Xu, G., Kokiko-Cochran, O.N., Roy, S.M., Van Eldik, L.J., et al., 2016. Selective suppression of the alpha isoform of p38 MAPK rescues late-stage tau pathology. Alzheimer's Res. Ther. 8 (1), 54.
Mathis, D.M., Furman, J.L., Norris, C.M., 2011. Preparation of acute hippocampal slices from rats and transgenic mice for the study of synaptic alterations during aging and amyloid pathology. J. Vis. Exp. (49).
Oakley, H., Cole, S.L., Logan, S., Maus, E., Shao, P., Craft, J., et al., 2006. Intraneuronal beta-amyloid aggregates, neurodegeneration, and neuron loss in transgenic mice with five familial Alzheimer's disease mutations: potential factors in amyloid plaque formation. J. Neurosci. 26 (40), 10129–10140.
Obeid, R., Herrmann, W., 2006. Mechanisms of homocysteine neurotoxicity in neurodegenerative diseases with special reference to dementia. FEBS Lett. 580 (13), 2994–3005.
O'Leary, T.P., Brown, R.E., 2022. Visuo-spatial learning and memory impairments in the 5xFAD mouse model of Alzheimer's disease: effects of age, sex, albinism, and motor impairments. Genes Brain Behav 21 (4), e12794.
Prins, N.D., Harrison, J.E., Chu, H.M., Blackburn, K., Alam, J.J., Scheltens, P., et al., 2021. A phase 2 double-blind placebo-controlled 24-week treatment clinical study of the p38 alpha kinase inhibitor neflamapimod in mild Alzheimer's disease. Alzheimer's Res. Ther. 13 (1), 106.
Provencher, S.W., 1993. Estimation of metabolite concentrations from localized in vivo proton NMR spectra. Magn. Reson. Med. 30 (6), 672–679.
Raza, A., Crothers, J.W., McGill, M.M., Mawe, G.M., Teuscher, C., Krementsov, D.N., 2017. Anti-inflammatory roles of p38alpha MAPK in macrophages are context dependent and require IL-10. J. Leukoc. Biol. 102 (5), 1219–1227.
Roy, S.M., Grum-Tokars, V.L., Schavocky, J.P., Saeed, F., Staniszewski, A., Teich, A.F., et al., 2015. Targeting human central nervous system protein kinases: an isoform selective p38alphaMAPK inhibitor that attenuates disease progression in Alzheimer's disease mouse models. ACS Chem. Neurosci. 6 (4), 666–680.
Roy, S.M., Minasov, G., Arancio, O., Chico, L.W., Van Eldik, L.J., Anderson, W.F., et al., 2019. A selective and brain penetrant p38alphaMAPK inhibitor candidate for neurologic and neuropsychiatric disorders that attenuates neuroinflammation and cognitive dysfunction. J. Med. Chem. 62 (11), 5298–5311.
Scheltens, P., Prins, N., Lammertsma, A., Yaqub, M., Gouw, A., Wink, A.M., et al., 2018. An exploratory clinical study of p38alpha kinase inhibition in Alzheimer's disease. Ann Clin Transl Neurol 5 (4), 464–473.
Sil, A., Erfani, A., Lamb, N., Copland, R., Riedel, G., Platt, B., 2022. Sex differences in behavior and molecular pathology in the 5XFAD model. J Alzheimers Dis 85 (2), 755–778.
Sudduth, T.L., Powell, D.K., Smith, C.D., Greenstein, A., Wilcock, D.M., 2013. Induction of hyperhomocysteinemia models vascular dementia by induction of cerebral microhemorrhages and neuroinflammation. J Cereb Blood Flow Metab 33 (5), 708–715.
Sudduth, T.L., Weekman, E.M., Brothers, H.M., Braun, K., Wilcock, D.M., 2014. beta-amyloid deposition is shifted to the vasculature and memory impairment is exacerbated when hyperhomocysteinemia is induced in APP/PS1 transgenic mice. Alzheimer's Res. Ther. 6 (3), 32.
Targa Dias Anastacio, H., Matosin, N., Ooi, L., 2022. Neuronal hyperexcitability in Alzheimer's disease: what are the drivers behind this aberrant phenotype? Transl. Psychiatry 12 (1), 257.
Toledo, J.B., Arnold, S.E., Raible, K., Brettschneider, J., Xie, S.X., Grossman, M., et al., 2013. Contribution of cerebrovascular disease in autopsy confirmed neurodegenerative disease cases in the National Alzheimer's Coordinating Centre. Brain 136 (Pt 9), 2697–2706.
Van Eldik, L.J., Carrillo, M.C., Cole, P.E., Feuerbach, D., Greenberg, B.D., Hendrix, J.A., et al., 2016. The roles of inflammation and immune mechanisms in Alzheimer's disease. Alzheimers Dement (N Y) 2 (2), 99–109.
Wu, M., Zhang, M., Yin, X., Chen, K., Hu, Z., Zhou, Q., et al., 2021. The role of pathological tau in synaptic dysfunction in Alzheimer's diseases. Transl. Neurodegener. 10 (1), 45.
Zhou, Z., Bachstetter, A.D., Spani, C.B., Roy, S.M., Watterson, D.M., Van Eldik, L.J., 2017. Retention of normal glia function by an isoform-selective protein kinase inhibitor drug candidate that modulates cytokine production and cognitive outcomes. J. Neuroinflammation 14 (1), 75.